Interfacial Topochemical Fluoridation of $MAPbI_3$ by Fluoropolymers

Benjamin M. Lefler[1], Theodore J. Houser[2], Arkita Chakrabarti[2], Steven J. May[1*], and Aaron T. Fafarman[2*]
[1]Department of Materials Science and Engineering, Drexel University, Philadelphia, PA 19104
[2]Department of Chemical and Biological Engineering, Drexel University, Philadelphia, PA 19104

ORCiDs:
B.M.L.: 0000-0003-0205-8479
A.C.: 0000-0002-6597-3503
S.J.M.: 0000-0002-8097-1549
A.T.F.: 0000-0003-3652-3383

*corresponding authors
E-mails:
smay@drexel.edu
fafarman@drexel.edu

Abstract:

Herein it is demonstrated that under conditions relevant to perovskite synthesis (>140 °C in air), fluoride can topochemically react across the interface between a halide perovskite and a fluoropolymer when in close contact, thereby creating a small quantity of strongly bonded lead fluoride species. The quantity increases with temperature and processing duration. Photo-induced charge carrier lifetime provides a metric for the resulting changes in electronic structure of the perovskite. Under short-duration and/or moderate temperature processing, fluoride transfer to the perovskite yields increased carrier lifetimes, up to three-fold longer than control samples, which is attributed to passivation of surface defects. Under more forcing conditions, the trend reverses: excessive fluoridation leads to shortened carrier lifetimes, which is ascribed to substantial interfacial formation of PbF_2. It is demonstrated that an interface with bulk crystalline PbF_2 quenches perovskite photoluminescence, likely due to PbF_2 serving as an electron acceptor for the conduction band of $MAPbI_3$.

ToC Graphic

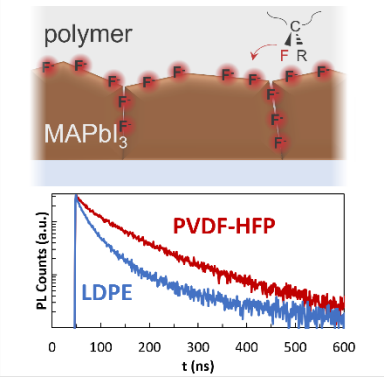

Main Text:

Physical contact between any two chemically distinct materials creates the potential for interfacial reactions, which are often poorly understood or not recognized at all yet can lead to significant alterations to the electronic structure of one or both materials. Knowledge of the existence and extent of solid-state interfacial reactions as a function of synthesis conditions is critical for photovoltaic devices, which consist of multiple interfaces that are critical to their function, e.g. between absorber layer and transport layer. In bulk composite materials composed of any two interspersed yet chemically distinct phases, the opportunity for reaction is even greater, as a consequence of the increased surface area. While such interfaces are often imagined as abrupt discontinuities in composition, in reality reactions between chemically distinct phases can lead to significant intermixing of their atomic components[1,2]. The propensity for such solid-state reactions might be especially high in the promising next-generation photovoltaic materials known as metal halide perovskites, due to the well-known high diffusivity of their constituent ions[3].

Lead halide perovskites are at the forefront of photovoltaic materials research, owing to excellent optoelectronic properties such as suitable bandgaps for efficient solar conversion, high absorption coefficients, long carrier lifetimes/diffusion lengths, and small exciton binding energies, as well as earth-abundance and low-cost solution processibility[4–6]. Despite boasting bulk defect tolerance[7], surfaces and grain boundaries are sites of non-radiative recombination[8–13]. Additionally, surfaces offer initiating sites for degradation. The archetypal photovoltaic perovskite, methylammonium lead triiodide, $MAPbI_3$ (methylammonium, $MA^+ = CH_3NH_3^+$), is especially prone to such degradation: phase separation to PbI_2 and volatile MAI initiates at the grain surface and proceeds into the grain interior layer-by-layer[14]. Therefore, both device efficiency and stability can be improved by passivating grain surfaces with strongly-bonding species, which many studies have explored by using additives with strongly coordinating moieties, i.e. Lewis bases, which bind to the perovskite surface[8,15–20].

Recently, fluoride has been studied as an effective surface-terminating ion for perovskite materials; typically incorporation is achieved by inclusion of alkali fluoride salts in the perovskite precursor solution, resulting in enhanced carrier lifetimes and phase stability due to passivation[21–23]. In this sense, fluoride behaves similarly to the more broadly studied chloride additive, which is excluded from the perovskite bulk and passivates grain boundaries and surfaces[8,24–27]. Like chloride, fluoride is too small to form a solid solution with iodide perovskites and is relegated to grain exteriors, where it is posited to bond to uncoordinated Pb^{2+}, form strong hydrogen bonds with the organic *A*-site cation, and stabilize the MAI-terminated surface[21]. Such stabilization of surface MAI could be beneficial because MAI-terminated surfaces are calculated to be less prone to deep-trap-state defects than otherwise-terminated perovskite surfaces[11]. However, fluorides have woefully poor solubility in typical perovskite precursor solvents such as *N,N*-dimethylformamide (DMF), and fluoride aggregates in precursor solutions can be detrimental to device performance, limiting the benefits of fluoride salt solution additives[28]. Alternatively, a post-deposition treatment can be a route to avoid these issues and achieve uniform surface passivation.

Fluoropolymers (a different potential source of fluoride, as we show below) have previously been incorporated into perovskite devices as barrier materials in the form of encapsulants[29], transport layers[30,31], and most notably as composites[32–39] with the perovskite absorber layer. Several studies also indicate that even when incorporated as composites, a significant volume of the fluoropolymer is expelled from the composite layer to form a superficial interlayer[38,39]. Such composites have been shown to improve film crystallization kinetics[32,38] and help to passivate perovskite grains through polar interactions with the C-F groups[35,37,38]. In those studies, incorporation of fluoropolymers demonstrated promising results for perovskite function and stability and the fluoropolymer-perovskite interface was reasonably

presumed to be inert; nonetheless, significant functionally relevant interfacial reactions are revealed in this work.

For two decades, topochemical fluoride incorporation into transition metal oxides has been demonstrated using fluoropolymer decomposition as the fluoride source[40,41], though more recently it has come to light that fluoride can be liberated from fluoropolymers to convert oxides to oxyfluorides at modest temperatures of 150-250 °C,[42–45] far below the reported decomposition temperatures of the polymers. In this work, we show that this same fluoridation chemistry occurs with halide perovskites. We measure interfacial reactions in two different perovskite/fluoropolymer heterostructure architectures: interspersed composites made of poly(vinylidene fluoride) (PVDF) and $CsPbI_3$, and laminated layers of $MAPbI_3$ and poly(vinylidene fluoride-*co*-hexafluoropropylene) (PVDF-HFP). The laminated layers are an especially useful system for both their well-defined spatial arrangement of the fluoride source relative to the perovskite and for the ability to delaminate and thus expose the interface after reaction. We find that fluoride can be transferred to the perovskite surface at temperatures above 140 °C in air, leading to an up-to-3-fold enhancement in effective photo-induced charge-carrier lifetime. At higher temperatures and longer treatment times, a PbF_2 phase forms on the surface of $MAPbI_3$, accompanied by carrier quenching. Study of a polymer-free model system of $MAPbI_3$ supported on polycrystalline PbF_2 suggests that quenching is driven by electron extraction to the PbF_2.

First, the temperature threshold and environmental conditions necessary for fluoride transfer from PVDF to lead halide perovskite materials were investigated with $CsPbI_3$-PVDF composite films and X-ray photoelectron spectroscopy (XPS). Covalently-bonded organo-fluorine and ionic fluoride can be distinguished using XPS, with ionic fluoride presenting a lower 1*s* binding energy than that of organo-fluorine. $CsPbI_3$ was employed for this part of the study to avoid issues of volatility posed by $MAPbI_3$, both during the high temperature processing and under the ultra-high vacuum and high-energy irradiative conditions of XPS[46]. Composite films of $CsPbI_3$-PVDF were prepared by spin-coating 0.55 M $CsPbI_3$ in 10 mg/mL PVDF-DMF solution. One set of these films were heated on a hotplate at various temperatures from 100 °C to 200 °C for 1h in ambient atmosphere, while a second set were annealed in a nitrogen-filled glovebox, and XPS was then measured. The high-resolution spectral data obtained at the F 1*s* region are shown in **Figure S1**. In the set of films annealed in air, the organo-fluorine peak corresponding to the -CH_2CF_2- monomer of PVDF was measured at a binding energy of ~688.8 eV while the ionic fluoride peak appeared at ~684.2 eV for treatment temperatures at or above 140 °C, indicating the temperature threshold for fluoride liberation from PVDF. Meanwhile, no significant signal for ionic fluoride was observed in films heated in nitrogen atmosphere, regardless of temperature. This is interesting to consider in light of the fact that oxide films *are* fluoridated by fluoropolymers in inert atmosphere[47]. In both examples of successful fluoridation, oxygen is present: either atmospheric oxygen in the case of perovskite halides, or inherent oxygen in the crystal as in the case of perovskite oxides. Therefore, we speculate that the driving force for fluoride liberation is oxidation of the carbon backbone. From these results, we conclude that the conditions required for fluoride liberation from PVDF-based fluoropolymers are temperatures of at least 140 °C and the presence of oxygen.

Having established the requisite temperature and atmosphere conditions for fluoride transfer from PVDF to the cesium-based iodide perovskite, we now turn exclusively to the study of lamination between PVDF and MA-based iodide perovskites. The lamination processing scheme is illustrated in **Figure 1a,b** and explained in depth in the Experimental Details section of the Supporting Information. In short, a stack including the spincast $MAPbI_3$ film on glass, polymer (polyolefins for control samples and PVDF-HFP for target samples), and glass superstrate are loaded into a heated die and annealed for a set

duration in a hydraulic press before applying pressure. The resultant sample is shown in **Figure 1c**, in which the polymer is laminated between the $MAPbI_3$ film and glass superstrate. **Figure 1d** illustrates our hypothesis for the microstructural and chemical effects that may occur during processing. During the lamination process, grains may grow due to thermal energy, and fluoride may be transferred (pictured in red) to the surface of the perovskite. As in the case of chloride-doped $MAPbI_3$ and as predicted by previous fluoride-doping work, fluoride is too small to be miscible with iodide perovskites and should therefore be relegated to the outside of grains as surface-terminating ions.

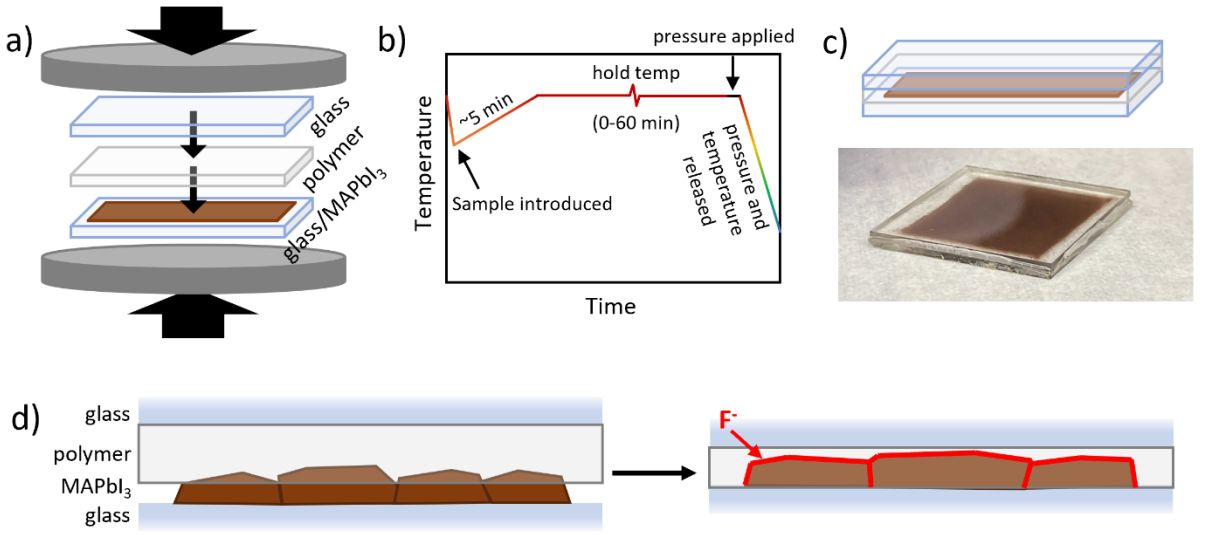

Figure 1. Lamination schematic and procedure. a) Schematic of laminate stack between the core dies of the hydraulic press. b) Polymer lamination procedure. A sample is introduced to a preheated die, during which the die temperature falls ~10 °C. The temperature returns to the desired temperature (~5 minutes) and is held for a set amount of time (0-60 min). Then 100 bar of pressure is applied until the pressure equilibrates (~20 seconds), after which the pressure and temperature are released. c) Schematic and picture of a laminated film. d) Representation of the hypothetical microstructural and chemical effects of lamination. Grains grow due to annealing, and fluoride is transferred to the perovskite surface from the fluoropolymer.

For a control data set, we established the contribution of the purely physical effects of applying heat, pressure, and melt-flow of a polymer to the perovskite structure (and hence photophysics). We performed laminations with two chemically inert polyolefins, low-density polyethylene (LDPE, T_{melt} ~ 110 °C) and polypropylene (PP, T_{melt} ~ 160 °C), at a range of temperatures and times. By comparing fluoropolymer-laminated samples to this baseline later in the study, we deconvolute the contribution of fluoridation chemistry from these concurrent effects. $MAPbI_3$ films were laminated at temperatures ranging from 150 °C to 210 °C, for treatment times ranging from 2 minutes to 60 minutes. **Figure 2a** shows the time-resolved photoluminescent (TRPL) decays of a set of films laminated with LDPE at different temperatures for 15 minutes, and **Figure 2b** shows TRPL decays of a set of films laminated with LDPE at 170 °C for different treatment times. Both sets show the improvement in carrier lifetime for treatments at increasing time and temperature. The effective carrier lifetime in each case was calculated as a weighted-average of a multi-exponential decay fitted curve as described in the Experimental Details section of the Supporting Information. The superset of all films' effective lifetimes is plotted in **Figure 2c**, as sorted into four temperature ranges: 150 °C, 170-175 °C, 185-190 °C, and 200-210 °C. TRPL decays for all samples are provided in **Figure S2**. As revealed through scanning electron microscopy (SEM), these control samples clearly exhibit consolidation of grains into larger and faceted crystallites with lower

overall grain boundary area (**Figure S3**). Specifically, we compared as-deposited films (unpressed) with films laminated with LDPE at 150 °C and 200 °C for 1h (which were subsequently manually delaminated) and observed evident grain consolidation at high temperature. Such morphological changes can be anticipated to enhance charge carrier lifetime. Dunlap-Shohl *et al.*[2] have previously investigated the dependence of grain growth on pressure-annealing conditions in $MAPbI_3$ films. Their work shows that grain growth kinetics are nearly independent of applied pressure but are a function of time and temperature as described by the Turnbull model for grain growth. By combining this Turnbull model with work by Adhyaksa *et al.*[48] on the dependence of effective carrier lifetime on grain size in perovskite films, we fit a model for the grain growth effect on carrier lifetimes, shown as the dashed lines in **Figure 2c**, to serve as a universal control across all time-temperature parameter space for comparison with chemical effects of fluoridation. Full details are included in **Note S1** of the Supporting Information**.**

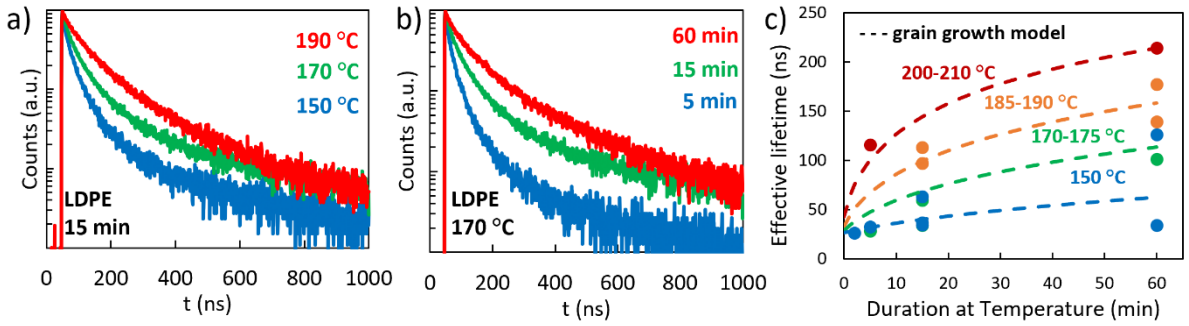

Figure 2. TRPL results of polyolefin lamination. a) TRPL decays of $MAPbI_3$ films laminated with LDPE for 15 minutes at various temperatures. b) TRPL decays of $MAPbI_3$ films laminated at 170 °C with various treatment durations. c) Effective TRPL lifetimes, calculated as weighted average lifetimes from bi- and tri-exponential fits, of $MAPbI_3$ films laminated with polyolefins LDPE or PP, plotted vs. lamination duration and sorted visually into four ranges of treatment temperatures: 150 °C (blue), 170-175 °C (green), 185-190 °C (orange), and 200-210 °C (red). Dashed lines represent the fit to the kinetic model for effective lifetime as a result of grain growth.

Fluoropolymer lamination experiments were performed with Solef® 21508, a commercial PVDF-HFP copolymer with T_{melt} ~ 135 °C. **Figure 3a** shows the effective carrier lifetime as a function of lamination duration for $MAPbI_3$ films laminated with PVDF-HFP in the four designated temperature ranges: 150 °C, 170-175 °C, 185-190 °C, and 200-210 °C. TRPL decays of all samples can be found in **Figure S4**. The appropriate curve from the grain-growth model in **Figure 2c** is included as a dashed line, representing our baseline expectation for microstructural effects alone, i.e. the anticipated effective lifetime when laminating with a polyolefin. Any enhancement in lifetime in excess of that expected from the grain-growth model is specific to differences between the fluoropolymer and the polyolefin control. Generalizing the results at all four temperatures in **Figure 3a**, we observe that lifetime is not a monotonic function of lamination time: maxima are observed at early times that exceed the expectations from grain-growth alone, followed by deteriorating lifetime. Specifically, both of the lower temperature ranges, 150 °C and 170-175 °C, show trends that maximize effective lifetime with 30-minute treatments, achieving median effective lifetimes of 134 and 132 ns, respectively, with respective increases of 170% and 50% *versus* the grain-growth model. All treatment durations t ≤ 30 min for these temperature ranges result in film lifetimes that outperform the grain-growth model. The higher temperature ranges, 185-190 °C and 200-210 °C, reach their maxima at shorter treatment times: 105 ns (5 minutes) and 122 ns (0 minutes), respectively, outperforming the grain growth model. (Note that all samples are subject to 5 minutes of

thermal equilibration prior to lamination, including the '0 minute' examples.) Under the combination of high temperature and long duration, the average lifetimes are significantly degraded, underperforming the expectation of the grain-growth model by several fold. **Figure 3a** provides a clear indicator of the existence of a competition between a beneficial effect at low temperature/short duration and a detrimental effect under more forcing conditions. The fluoropolymer possesses similar physical properties (e.g. melting temperature) to the polyolefin controls, so we turned to XPS to understand chemical changes accompanying the above observations. Specifically, to test whether this fluoropolymer-specific enhancement/deterioration correlates with fluoridation, high-resolution F 1*s* spectra from XPS were taken, demonstrating that fluoride does transfer to the perovskite with these treatments (**Figure 3b**). $MAPbI_3$ films laminated with PVDF-HFP under conditions of 5 minutes at 150 °C (left), 15 minutes and 170 °C (center), and 60 minutes at 200 °C (right) were manually delaminated and measured. Evidence of ionic fluoride (binding energy ~685.3 eV) was present at even the gentlest condition used of 5 minutes at 150 °C, with increasing fluoride signal present for lamination conditions of higher temperature and longer duration.

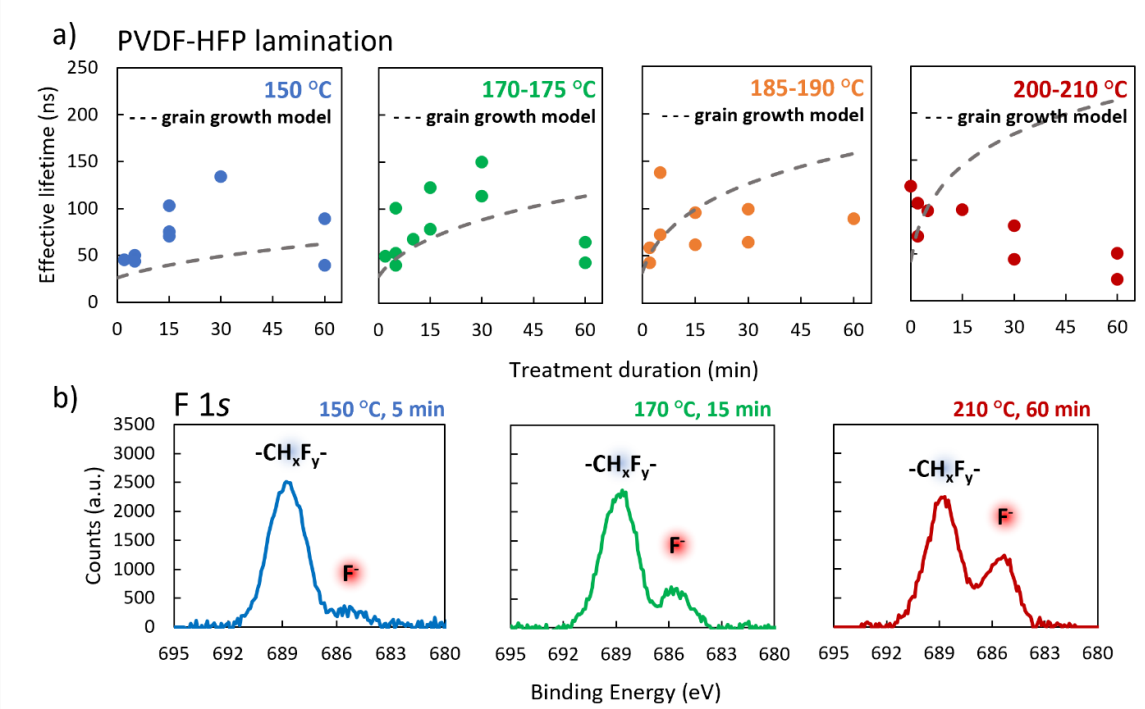

Figure 3. a) Effects of PVDF-HFP lamination on $MAPbI_3$ carrier lifetime. Effective lifetimes calculated from fitting TRPL decays to bi- or tri-exponentials for $MAPbI_3$ films laminated for various durations at each of the four temperature ranges. Also shown in each plot for comparison is the prediction for effective lifetime from the grain-growth kinetic model, represented as dashed lines. b) XPS high-resolution F 1*s* spectra measured from films laminated (then manually delaminated) with PVDF-HFP at various conditions. Organo-fluorine signal appears at binding energy ~688.7 eV. Fluoride signal appears at binding energy ~685.3 eV.

Given the correlation of the highest carrier lifetime with the observation of a small quantity of anionic fluoride, we ascribe the beneficial effect of fluoropolymer lamination to topochemical replacement of a limited number of surface lead-iodide bonds with lead-fluoride. Overall, these results are technologically promising: a low temperature, low duration processing window is especially pertinent as lamination conditions in, for example, PV devices are limited by the stability of other layers, i.e. charge

transport layers, and particularly of the possible interfacial reactivity between charge transport layers and the perovskite[2].

Previous studies which used alkali fluoride additives in perovskite precursor solutions determined an optimal concentration to be on the order of 0.1 mol %, with higher amounts hurting device performance[21,22], though a detailed mechanism has not yet been offered, to our knowledge. In the case of a LiF additive, higher concentrations increased hysteresis in completed solar cells, likely due to the high mobility of the added Li ions[22]. As previously mentioned, another mechanism of device inefficiency at higher concentrations may be fluoride aggregation due to the poor solubility of alkali fluorides in aprotic organic solvents like DMF and dimethyl sulfoxide (DMSO)[28]. However, the topochemical fluoridation approach in this work does not introduce extra cations to the material, and as a solid-state treatment, it is not subject to aggregation due to insolubility. Therefore, to understand the mechanism of this lifetime quenching behavior for treatments longer than the temperature-dependent optimal duration, we laminated a $MAPbI_3$ film with PVDF-HFP at 210 °C for 1h, then manually delaminated the stack to investigate the resultant perovskite film. The X-ray diffraction (XRD) pattern of the film (**Figure 4**) reveals small peaks at ~26.3, and ~30.1 degrees in 2θ which can be attributed to PbF_2, indicating that given sufficient time and temperature, the fluoropolymer can convert enough lead from $MAPbI_3$ to PbF_2 for a X-ray scattering peak to be observed. Interestingly, lanthanide spectroscopy has revealed a surprisingly deep conduction band edge for PbF_2 with a binding energy of about -4.0 eV *versus* the vacuum level[49], while that of $MAPbI_3$ has been determined to be about -3.9 eV[50,51]. While these energy levels can be somewhat dependent on chemical environment[52], it raises the possibility of electron injection from the conduction band of $MAPbI_3$ into the conduction band of PbF_2.

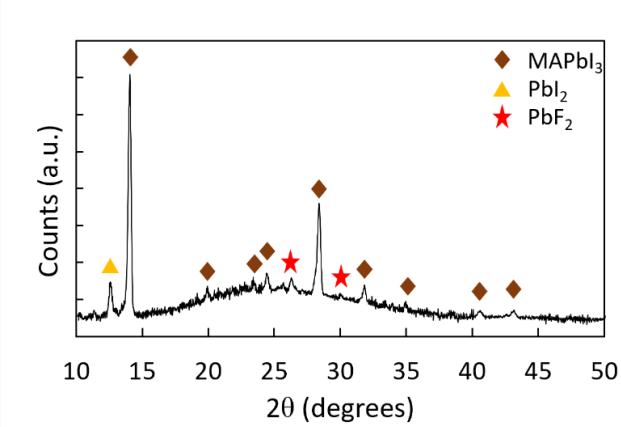

Figure 4. XRD of $MAPbI_3$ film after fluoropolymer lamination with PVDF-HFP under conditions of 210 °C, 1h. The film was delaminated and measured.

In light of this, we prepared substrates of polycrystalline PbF_2 and CaF_2 by compressing the respective powders using a hydraulic press into freestanding pellets, and then subsequently deposited $MAPbI_3$ on them by drop-casting. CaF_2 was chosen as a control substrate for having chemical similarity as a binary fluoride, with a conduction band edge at ~-0.5 eV which is well above that of $MAPbI_3$ and therefore prevents any charge transfer[49]. The TRPL data from these samples are shown in **Figure 5a**, showing fast carrier quenching in the case of $MAPbI_3$ on PbF_2 substrates (τ_{avg} = 15.4 ns) compared to $MAPbI_3$ on CaF_2 (τ_{avg} = 159 ns). This quenching is evident in ~30-fold greater steady-state PL (SSPL) emission intensity for $MAPbI_3$ on the CaF_2 substrate than on PbF_2, as seen in **Figure 5b** (left). This suggests

the existence of rapid charge-transfer from $MAPbI_3$ to PbF_2. Additionally, while $MAPbI_3$ on CaF_2 demonstrates the usual single emission peak, a closer look at $MAPbI_3$ on PbF_2 reveals emission at two distinct wavelengths, 750 nm and 800 nm (**Figure 5b,** right). **Figure 5c** displays the TRPL decays measured for each emission at times very shortly after the excitation pulse. The emission at 750 nm is the expected characteristic response of carriers excited by a sub-ns pulse width followed by exponential decay. However, TRPL data measured for 800 nm emission shows an initial *increase* in PL intensity after the excitation before then decaying, represented in **Figure 5c** by the dashed lines and arrow showing the delay in intensity maximum. We speculate that this intriguing behavior could result from carriers transferred into PbF_2 being injected back into low-lying band-tail states of the $MAPbI_3$, as illustrated by **Figure 5d**. In this scenario, the 750 nm emission originates from typical band-edge recombination in $MAPbI_3$ that occurs very soon after excitation, before charge transfer to PbF_2 or energy migration into the band-tail states has a chance to occur. Meanwhile, the red-shifted 800 nm emission originates from $MAPbI_3$ band-tail states, such as have been documented elsewhere[53], that may have been repopulated by the PbF_2 acceptor. Therefore, the kinetics of charge injection into PbF_2 and subsequent repopulation of $MAPbI_3$ band-tail states accounts for the delay in the band-tail population maximum (and therefore emission maximum) after the excitation pulse. The round-trip energy loss is approximately 100 meV in this scenario, indicating a close alignment of the PbF_2 and $MAPbI_3$ conduction bands. Alternatively, the band-tail states might be slowly populated directly from the band-edge carriers in $MAPbI_3$ itself, in which case their longer lifetime suggests that they are too low energy to inject into the PbF_2, again implying an alignment with less than 100 meV of offset.

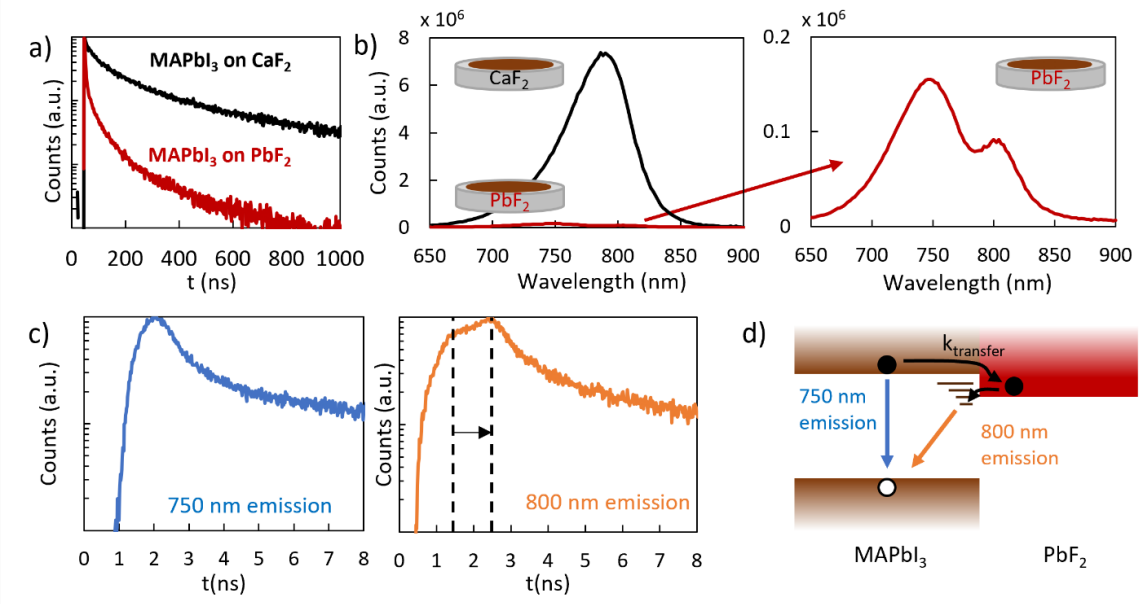

Figure 5. Effects of PbF_2 on $MAPbI_3$ carrier kinetics measured from $MAPbI_3$ drop-cast on pelleted substrates of PbF_2 and CaF_2 control. a) TRPL decays of $MAPbI_3$ on fluoride pellet substrates. Each decay shown is an average of decays from triplicate samples. b) SSPL emission spectra of $MAPbI_3$ on fluoride pellet substrates shown on the same intensity scale (left), and enlarged to focus on the $MAPbI_3/PbF_2$ spectrum (right). c) High-resolution TRPL data of the initial decay of $MAPbI_3$ on PbF_2 measured for 750 nm emission (left) and 800 nm emission (right). Dashed lines and arrow indicate the sub-ns delay in decay maximum intensity. d) Band diagram illustration of the proposed emission pathways from $MAPbI_3$ on PbF_2. The 750 nm emission stems from $MAPbI_3$ band-to-band recombination. The 800 nm emission stems from interfacial recombination after electron transfer from the conduction band of $MAPbI_3$ to that of PbF_2, with interfacial charge transfer from $MAPbI_3$ to PbF_2 causing the delay in TRPL intensity maximum.

To our knowledge, PbF_2 has only been incorporated into perovskite solar cell materials once before, as a sub-nm-thickness passivating layer between the perovskite and electron transport material (ETM) SnO_2[54], and it has never been identified as a possible electron acceptor from $MAPbI_3$ or related halide perovskites. However, through DFT calculations, Feng *et al.*[55] reported that PbF_2 is expected to effectively stabilize the $MAPbI_3$ interface through slightly compressive lattice matching, strong binding energy, and rearrangement of the perovskite surface to favor MAI-layer termination which also presents larger barriers to deep-trap surface defects than perovskite surfaces with other termination layers[11].

In this work, we demonstrated that PVDF-HFP fluoropolymer lamination processing can chemically alter the surface of $MAPbI_3$ through fluoridation at temperatures exceeding 140 °C in air. Using polyolefin lamination as a control for determining the effects of thermally-activated grain growth on effective carrier lifetime, we observed that fluoridation by polymer lamination can lead to up to ~3-fold longer carrier lifetimes compared to the controls. For a given lamination temperature, the duration of treatment can be optimized for a maximum effective carrier lifetime, while treatments longer than the optimal duration cause carrier quenching, which we attribute to PbF_2 formation and electron transfer from $MAPbI_3$ to PbF_2. Our results indicate that the surface fluoridation achieved during fluoropolymer lamination is a kinetically controlled process, by which there is an optimal extent of fluoridation to provide passivating effects – whether by binding superficial Pb^{2+} in the perovskite structure with terminal fluoride, or by conversion of a sufficiently thin layer of perovskite to PbF_2 – while longer times and higher temperatures facilitate the formation of substantial PbF_2. These results provide valuable insight that can inform future perovskite processing with fluoropolymer perovskite additives and interlayers, particularly among formamidinium-based perovskites which commonly involve annealing temperatures of >150 °C[56,57]. These results are also of interest for the more nascent focus of perovskite solar cell lamination processing[2,58–61].

Supporting Information:
Experimental details, High resolution XPS of $CsPbI_3$-PVDF composite films heated in air and in N_2, TRPL decays of polyolefin-laminated $MAPbI_3$ films, SEM images of $MAPbI_3$ films after various polyolefin lamination conditions, TRPL decays of PVDF-HFP-laminated $MAPbI_3$ films, discussion of the grain growth model.

Conflicts of Interest:
The authors declare no conflicts of interest.

Acknowledgements:
B.M.L. and S.J.M. were supported by the National Science Foundation Grant No. CMMI- 2001888. T.J.H., A.C., and A.T.F. were supported by National Science Foundation Grant No. DMR-1847952**.** SEM, XRD and XPS analyses were performed using instruments in the Materials Characterization Core at Drexel University. We thank Prof. Cherie Kagan (U. of Pennsylvania) for access to the fluorescent spectrometer for photoluminescence measurements.

References

(1) Jahn, U.; Okamoto, T.; Yamada, A.; Konagai, M. Doping and Intermixing in CdS/CdTe Solar Cells Fabricated under Different Conditions. *J Appl Phys* **2001**, *90*, 2553–2558.

(2) Dunlap-Shohl, W. A.; Li, T.; Mitzi, D. B. Interfacial Effects during Rapid Lamination within $MAPbI_3$ Thin Films and Solar Cells. *ACS Appl Energy Mater* **2019**, *2*, 5083–5093.

(3) Tress, W.; Marinova, N.; Moehl, T.; Zakeeruddin, S. M.; Nazeeruddin, M. K.; Grätzel, M. Understanding the Rate-Dependent J–V Hysteresis, Slow Time Component, and Aging in $CH_3NH_3PbI_3$ Perovskite Solar Cells: The Role of a Compensated Electric Field. *Energy Environ Sci* **2015**, *8*, 995–1004.

(4) Jena, A. K.; Kulkarni, A.; Miyasaka, T. Halide Perovskite Photovoltaics: Background, Status, and Future Prospects. *Chem Rev* **2019**, *119*, 3036–3103.

(5) Yin, W.-J.; Yang, J.-H.; Kang, J.; Yan, Y.; Wei, S.-H. Halide Perovskite Materials for Solar Cells: A Theoretical Review. *J Mater Chem A Mater* **2015**, *3*, 8926–8942.

(6) Dunlap-Shohl, W. A.; Zhou, Y.; Padture, N. P.; Mitzi, D. B. Synthetic Approaches for Halide Perovskite Thin Films. *Chem Rev* **2019**, *119*, 3193–3295.

(7) Yin, W.-J.; Shi, T.; Yan, Y. Unusual Defect Physics in $CH_3NH_3PbI_3$ Perovskite Solar Cell Absorber. *Appl Phys Lett* **2014**, *104*, 063903.

(8) deQuilettes, D. W.; Vorpahl, S. M.; Stranks, S. D.; Nagaoka, H.; Eperon, G. E.; Ziffer, M. E.; Snaith, H. J.; Ginger, D. S. Impact of Microstructure on Local Carrier Lifetime in Perovskite Solar Cells. *Science* **2015**, *348*, 683–686.

(9) Ni, Z.; Bao, C.; Liu, Y.; Jiang, Q.; Wu, W.-Q.; Chen, S.; Dai, X.; Chen, B.; Hartweg, B.; Yu, Z.; Holman, Z.; Huang, J. Resolving Spatial and Energetic Distributions of Trap States in Metal Halide Perovskite Solar Cells. *Science* **2020**, *367*, 1352–1358.

(10) Haruyama, J.; Sodeyama, K.; Han, L.; Tateyama, Y. Termination Dependence of Tetragonal $CH_3NH_3PbI_3$ Surfaces for Perovskite Solar Cells. *J Phys Chem Lett* **2014**, *5*, 2903–2909.

(11) Uratani, H.; Yamashita, K. Charge Carrier Trapping at Surface Defects of Perovskite Solar Cell Absorbers: A First-Principles Study. *J Phys Chem Lett* **2017**, *8*, 742–746.

(12) Kong, W.; Ding, T.; Bi, G.; Wu, H. Optical Characterizations of the Surface States in Hybrid Lead–Halide Perovskites. *Physical Chemistry Chemical Physics* **2016**, *18*, 12626–12632.

(13) Shan, W.; Saidi, W. A. Segregation of Native Defects to the Grain Boundaries in Methylammonium Lead Iodide Perovskite. *J Phys Chem Lett* **2017**, *8*, 5935–5942.

(14) Fan, Z.; Xiao, H.; Wang, Y.; Zhao, Z.; Lin, Z.; Cheng, H. C.; Lee, S. J.; Wang, G.; Feng, Z.; Goddard, W. A.; Huang, Y.; Duan, X. Layer-by-Layer Degradation of Methylammonium Lead Tri-Iodide Perovskite Microplates. *Joule* **2017**, *1*, 548–562.

(15) Zuo, L.; Guo, H.; DeQuilettes, D. W.; Jariwala, S.; De Marco, N.; Dong, S.; DeBlock, R.; Ginger, D. S.; Dunn, B.; Wang, M.; Yang, Y. Polymer-Modified Halide Perovskite Films for Efficient and Stable Planar Heterojunction Solar Cells. *Sci Adv* **2017**, *3*, e1700106.

(16) Zhao, S.; Xie, J.; Cheng, G.; Xiang, Y.; Zhu, H.; Guo, W.; Wang, H.; Qin, M.; Lu, X.; Qu, J.; Wang, J.; Xu, J.; Yan, K. General Nondestructive Passivation by 4-Fluoroaniline for Perovskite Solar Cells with Improved Performance and Stability. *Small* **2018**, *14*, 1803350.

(17) Hsieh, C.-M.; Liao, Y.-S.; Lin, Y.-R.; Chen, C.-P.; Tsai, C.-M.; Wei-Guang Diau, E.; Chuang, S.-C. Low-Temperature, Simple and Efficient Preparation of Perovskite Solar Cells Using Lewis Bases Urea

and Thiourea as Additives: Stimulating Large Grain Growth and Providing a PCE up to 18.8%. *RSC Adv* **2018**, *8*, 19610–19615.

(18) Stewart, R. J.; Grieco, C.; Larsen, A. V; Maier, J. J.; Asbury, J. B. Approaching Bulk Carrier Dynamics in Organo-Halide Perovskite Nanocrystalline Films by Surface Passivation. *J Phys Chem Lett* **2016**, *7*, 1148–1153.

(19) Wang, F.; Geng, W.; Zhou, Y.; Fang, H.-H.; Tong, C.-J.; Loi, M. A.; Liu, L.-M.; Zhao, N. Phenylalkylamine Passivation of Organolead Halide Perovskites Enabling High-Efficiency and Air-Stable Photovoltaic Cells. *Advanced Materials* **2016**, *28*, 9986–9992.

(20) Zhang, H.; Nazeeruddin, M. K.; Choy, W. C. H. Perovskite Photovoltaics: The Significant Role of Ligands in Film Formation, Passivation, and Stability. *Advanced Materials* **2019**, *31*, 1805702.

(21) Li, N.; Tao, S.; Chen, Y.; Niu, X.; Onwudinanti, C. K.; Hu, C.; Qiu, Z.; Xu, Z.; Zheng, G.; Wang, L.; *et al*. Cation and Anion Immobilization through Chemical Bonding Enhancement with Fluorides for Stable Halide Perovskite Solar Cells. *Nat Energy* **2019**, *4*, 408–415.

(22) Yun, A. J.; Kim, J.; Gil, B.; Woo, H.; Park, K.; Cho, J.; Park, B. Incorporation of Lithium Fluoride Restraining Thermal Degradation and Photodegradation of Organometal Halide Perovskite Solar Cells. *ACS Appl Mater Interfaces* **2020**, *12*, 50418–50425.

(23) Lefler, B. M.; May, S. J.; Fafarman, A. T. Role of Fluoride and Fluorocarbons in Enhanced Stability and Performance of Halide Perovskites for Photovoltaics. *Phys Rev Mater* **2020**, *4*, 120301.

(24) Chen, Q.; Zhou, H.; Fang, Y.; Stieg, A. Z.; Song, T.-B.; Wang, H.-H.; Xu, X.; Liu, Y.; Lu, S.; You, J.; *et al*. The Optoelectronic Role of Chlorine in $CH_3NH_3PbI_3$(Cl)-Based Perovskite Solar Cells. *Nat Commun* **2015**, *6*, 7269.

(25) Colella, S.; Mosconi, E.; Pellegrino, G.; Alberti, A.; Guerra, V. L. P.; Masi, S.; Listorti, A.; Rizzo, A.; Condorelli, G. G.; De Angelis, F.; Gigli, G. Elusive Presence of Chloride in Mixed Halide Perovskite Solar Cells. *J Phys Chem Lett* **2014**, *5*, 3532–3538.

(26) Unger, E. L.; Bowring, A. R.; Tassone, C. J.; Pool, V. L.; Gold-Parker, A.; Cheacharoen, R.; Stone, K. H.; Hoke, E. T.; Toney, M. F.; McGehee, M. D. Chloride in Lead Chloride-Derived Organo-Metal Halides for Perovskite-Absorber Solar Cells. *Chemistry of Materials* **2014**, *26*, 7158–7165.

(27) Yin, W.-J.; Chen, H.; Shi, T.; Wei, S.-H.; Yan, Y. Origin of High Electronic Quality in Structurally Disordered $CH_3NH_3PbI_3$ and the Passivation Effect of Cl and O at Grain Boundaries. *Adv Electron Mater* **2015**, *1*, 1500044.

(28) Xiang, H.; Liu, P.; Wang, W.; Ran, R.; Zhou, W.; Shao, Z. Sodium Fluoride Sacrificing Layer Concept Enables High-Efficiency and Stable Methylammonium Lead Iodide Perovskite Solar Cells. *J Mater Sci Technol* **2022**, *113*, 138–146.

(29) Hwang, I.; Jeong, I.; Lee, J.; Ko, M. J.; Yong, K. Enhancing Stability of Perovskite Solar Cells to Moisture by the Facile Hydrophobic Passivation. *ACS Appl Mater Interfaces* **2015**, *7*, 17330–17336.

(30) Jo, J. W.; Jung, J. W.; Wang, H.-W.; Kim, P.; Russell, T. P.; Jo, W. H. Fluorination of Polythiophene Derivatives for High Performance Organic Photovoltaics. *Chemistry of Materials* **2014**, *26*, 4214–4220.

(31) Jeong, I.; Jo, J. W.; Bae, S.; Son, H. J.; Ko, M. J. A Fluorinated Polythiophene Hole-Transport Material for Efficient and Stable Perovskite Solar Cells. *Dyes and Pigments* **2019**, *164*, 1–6.

(32) Zhang, S.; Lu, Y.; Lin, B.; Zhu, Y.; Zhang, K.; Yuan, N.-Y.; Ding, J.-N.; Fang, B. PVDF-HFP Additive for Visible-Light-Semitransparent Perovskite Films Yielding Enhanced Photovoltaic Performance. *Solar Energy Materials and Solar Cells* **2017**, *170*, 178–186.

(33) Valero, S.; Soria, T.; Marinova, N.; Delgado, J. L. Efficient and Stable Perovskite Solar Cells Based on Perfluorinated Polymers. *Polym Chem* **2019**, *10*, 5726–5736.
(34) Jia, E.; Wei, D.; Cui, P.; Ji, J.; Huang, H.; Jiang, H.; Dou, S.; Li, M.; Zhou, C.; Wang, W. Efficiency Enhancement with the Ferroelectric Coupling Effect Using P(VDF-TrFE) in CH3NH3PbI3 Solar Cells. *Advanced Science* **2019**, *6*, 1900252.
(35) Zhang, C.; Wang, Z.; Yuan, S.; Wang, R.; Li, M.; Jimoh, M. F.; Liao, L.; Yang, Y. Polarized Ferroelectric Polymers for High-Performance Perovskite Solar Cells. *Advanced Materials* **2019**, *31*, 1902222.
(36) Zarenezhad, H.; Askari, M.; Halali, M.; Solati, N.; Balkan, T.; Kaya, S. Enhanced Electron Transport Induced by a Ferroelectric Field in Efficient Halide Perovskite Solar Cells. *Solar Energy Materials and Solar Cells* **2020**, *206*, 110318.
(37) Sun, R.; Tian, Q.; Li, M.; Wang, H.; Chang, J.; Xu, W.; Li, Z.; Pan, Y.; Wang, F.; Qin, T. Over 24% Efficient Poly(Vinylidene Fluoride) (PVDF)-Coordinated Perovskite Solar Cells with a Photovoltage up to 1.22 V. *Adv Funct Mater* **2023**, *33*, 2210071.
(38) Li, G.; Su, Z.; Canil, L.; Hughes, D.; Aldamasy, M. H.; Dagar, J.; Trofimov, S.; Wang, L.; Zuo, W.; Jerónimo-Rendon, J. J.; *et al*. Highly Efficient P-i-n Perovskite Solar Cells That Endure Temperature Variations. *Science* **2023**, *379*, 399–403.
(39) Moriya, Y.; Ishikawa, R.; Akiyama, S.; Ueno, K.; Shirai, H. Self-Assembled Fluorinated Polymer Passivation Layer for Efficient Perovskite Thin-Film Solar Cells. *Chem Lett* **2020**, *49*, 87–90.
(40) Clemens, O.; Slater, P. R. Topochemical Modifications of Mixed Metal Oxide Compounds by Low-Temperature Fluorination Routes. *Reviews in Inorganic Chemistry* **2013**, *33*, 105–117.
(41) Hirai, D.; Sawai, O.; Nunoura, T.; Hiroi, Z. Facile Synthetic Route to Transition Metal Oxyfluorides via Reactions between Metal Oxides and PTFE. *J Fluor Chem* **2018**, *209*, 43–48.
(42) Moon, E. J.; Xie, Y.; Laird, E. D.; Keavney, D. J.; Li, C. Y.; May, S. J. Fluorination of Epitaxial Oxides: Synthesis of Perovskite Oxyfluoride Thin Films. *J Am Chem Soc* **2014**, *136*, 2224–2227.
(43) Katayama, T.; Chikamatsu, A.; Hirose, Y.; Takagi, R.; Kamisaka, H.; Fukumura, T.; Hasegawa, T. Topotactic Fluorination of Strontium Iron Oxide Thin Films Using Polyvinylidene Fluoride. *J. Mater. Chem. C* **2014**, *2*, 5350–5356.
(44) Wang, J.; Shin, Y.; Arenholz, E.; Lefler, B. M.; Rondinelli, J. M.; May, S. J. Effect of Fluoropolymer Composition on Topochemical Synthesis of $SrMnO_{3-\delta}F_{\gamma}$. *Phys Rev Mater* **2018**, *2*, 073407.
(45) Lefler, B. M.; Duchoň, T.; Karapetrov, G.; Wang, J.; Schneider, C. M.; May, S. J. Reconfigurable Lateral Anionic Heterostructures in Oxide Thin Films via Lithographically Defined Topochemistry. *Phys Rev Mater* **2019**, *3*, 073802.
(46) McGettrick, J. D.; Hooper, K.; Pockett, A.; Baker, J.; Troughton, J.; Carnie, M.; Watson, T. Sources of Pb(0) Artefacts during XPS Analysis of Lead Halide Perovskites. *Mater Lett* **2019**, *251*, 98–101.
(47) Moon, E. J.; Choquette, A. K.; Huon, A.; Kulesa, S. Z.; Barbash, D.; May, S. J. Comparison of Topotactic Fluorination Methods for Complex Oxide Films. *APL Mater* **2015**, *3*, 062511.
(48) Adhyaksa, G. W. P.; Brittman, S.; Āboliņš, H.; Lof, A.; Li, X.; Keelor, J. D.; Luo, Y.; Duevski, T.; Heeren, R. M. A.; Ellis, S. R.; *et al.* Understanding Detrimental and Beneficial Grain Boundary Effects in Halide Perovskites. *Advanced Materials* **2018**, *30*, 1804792.
(49) Dorenbos, P. Determining Binding Energies of Valence-Band Electrons in Insulators and Semiconductors via Lanthanide Spectroscopy. *Phys Rev B* **2013**, *87*, 035118.
(50) Calió, L.; Kazim, S.; Grätzel, M.; Ahmad, S. Hole-Transport Materials for Perovskite Solar Cells. *Angewandte Chemie International Edition* **2016**, *55*, 14522–14545.

(51) Lin, L.; Jones, T. W.; Yang, T. C.; Duffy, N. W.; Li, J.; Zhao, L.; Chi, B.; Wang, X.; Wilson, G. J. Inorganic Electron Transport Materials in Perovskite Solar Cells. *Adv Funct Mater* **2021**, *31*, 2008300.

(52) Miller, E. M.; Zhao, Y.; Mercado, C. C.; Saha, S. K.; Luther, J. M.; Zhu, K.; Stevanović, V.; Perkins, C. L.; van de Lagemaat, J. Substrate-Controlled Band Positions in $CH_3NH_3PbI_3$ Perovskite Films. *Phys. Chem. Chem. Phys.* **2014**, *16*, 22122–22130.

(53) Wright, A. D.; Milot, R. L.; Eperon, G. E.; Snaith, H. J.; Johnston, M. B.; Herz, L. M. Band-Tail Recombination in Hybrid Lead Iodide Perovskite. *Adv Funct Mater* **2017**, *27*, 1700860.

(54) Yuan, S.; Wang, J.; Yang, K.; Wang, P.; Zhang, X.; Zhan, Y.; Zheng, L. High Efficiency $MAPbI_{3-x}Cl_x$ Perovskite Solar Cell via Interfacial Passivation. *Nanoscale* **2018**, *10*, 18909–18914.

(55) Feng, X. X.; Liu, B.; Long, M.; Cai, M.; Peng, Y.; Yang, J. Improving Stability of Lead Halide Perovskite via PbF_2 Layer Covering. *J Phys Chem Lett* **2020**, *11*, 6266–6272.

(56) Pool, V. L.; Dou, B.; Van Campen, D. G.; Klein-Stockert, T. R.; Barnes, F. S.; Shaheen, S. E.; Ahmad, M. I.; van Hest, M. F. A. M.; Toney, M. F. Thermal Engineering of $FAPbI_3$ Perovskite Material via Radiative Thermal Annealing and in Situ XRD. *Nat Commun* **2017**, *8*, 14075.

(57) Li, Z.; Yang, M.; Park, J.-S.; Wei, S.-H.; Berry, J. J.; Zhu, K. Stabilizing Perovskite Structures by Tuning Tolerance Factor: Formation of Formamidinium and Cesium Lead Iodide Solid-State Alloys. *Chemistry of Materials* **2016**, *28*, 284–292.

(58) Dunfield, S. P.; Moore, D. T.; Klein, T. R.; Fabian, D. M.; Christians, J. A.; Dixon, A. G.; Dou, B.; Ardo, S.; Beard, M. C.; Shaheen, S. E.; *et al.* Curtailing Perovskite Processing Limitations via Lamination at the Perovskite/Perovskite Interface. *ACS Energy Lett* **2018**, *3*, 1192–1197.

(59) Li, T.; Dunlap-Shohl, W. A.; Mitzi, D. B. Bifacial Perovskite Solar Cells via a Rapid Lamination Process. *ACS Appl Energy Mater* **2020**, *3*, 9493–9497.

(60) Schmager, R.; Roger, J.; Schwenzer, J. A.; Schackmar, F.; Abzieher, T.; Malekshahi Byranvand, M.; Abdollahi Nejand, B.; Worgull, M.; Richards, B. S.; Paetzold, U. W. Laminated Perovskite Photovoltaics: Enabling Novel Layer Combinations and Device Architectures. *Adv Funct Mater* **2020**, *30*, 1907481.

(61) Trinh, X.-L.; Kim, H.-C. Fully Solution-Processed Perovskite Solar Cells Fabricated by Lamination Process with Silver Nanoparticle Film as Top Electrode. *Energy Reports* **2020**, *6*, 1297–1303.